DE GRUYTER Open Physics 2024; 22: 20230166

Research Article

Benqiang Wang, Denglin Han, Wei Lin*, Xin Nie, Chenchen Wang, and Jizhen Zhang

Microscopic seepage simulation of gas and water in shale pores and slits based on VOF

https://doi.org/10.1515/phys-2023-0166
received September 05, 2023; accepted December 04, 2023

Abstract: The microscopic pore-fracture structure and wettability have a significant influence on the two-phase seepage of shale gas and water. Due to the limitation of experimental conditions, the seepage patterns of gas and water in shale pores and slits under different wetting conditions have not been clarified yet. In this study, the three-dimensional digital rock models of shale inorganic pores, organic pores, and microfractures are established by focused ion beam-scanning electron microscopy scanning, and gas-driven water seepage simulation in shale microscopic pore-fracture structure under different wetting conditions is carried out based on volume of fluid method. The simulation results show that the gas–water relative permeability curves of microfractures are up-concave, and the gas–water relative permeability curves of inorganic and organic pores are up-convex; the gas–water two-phase percolation in microfractures is least affected by the change of wettability, the gas–water two-phase percolation in inorganic pores is most affected by the change of wettability, and the organic pores are in between; the gas–water two-phase percolation zone of microfractures is the largest, and the isotonic saturation is the highest; under the water-wet conditions, the critical gas saturation of microfractures, inorganic pores, and organic pores are 0.13, 0.315, and 0.34, respectively, and the critical gas saturation of organic pores under non-water-wet conditions is 0.525, indicating that under water-bearing conditions, the shale gas flow capacity in water-wet microfractures is the strongest, followed by water-wet inorganic pores, water-wet organic pores, and hydrophobic organic pores, respectively.

Keywords: shale, microscopic pore-fracture, gas–water two-phase percolation, VOF, wettability

1 Introduction

Currently, marine shale gas in the southern Sichuan region holds a crucial position in China's shale gas exploration and development strategy. The Lower Silurian Longmaxi Formation is known for its high-quality shale, which has garnered extensive research and attention [1–3]. The Longmaxi Formation shale is characterized by its ancient age and multiple tectonic events, resulting in deep burial, high differential stress, pronounced reservoir heterogeneity, and significant variations in individual well production. The development models and techniques used in North America and other regions are not entirely applicable due to the challenges involved in shale gas development [4–6]. Taking the Weiyuan Block shale gas project of China Petroleum Group Chuanqing Drilling Engineering Co., Ltd. as an example, by the end of June 2021, a total of 202 producing wells have been drilled, with cumulative gas production reaching 7.9 billion cubic meters, and a recovery factor of only 4.8%. The overall decline rate of gas wells in the first year is as high as 60%, with an extended low-production period. Compared to conventional natural gas, shale gas exhibits characteristics such as low porosity, low permeability, low pressure, complex pore structure, and high clay content, requiring the utilization of horizontal drilling and large-scale hydraulic fracturing techniques for commercialization. After hydraulic fracturing in Weiyuan shale gas wells, the fluid recovery rate is approximately 51.3%, with a significant amount of fracturing fluid retained in the shale reservoir. Production data from foreign shale gas wells also indicate an average fluid recovery rate of 35 to 62% one year after production, with a substantial amount of fracturing fluid remaining in the formation. The water content in hydraulic fracturing fluids is typically greater than 90%. The presence of water in shale reservoirs has a significant

---

*** Corresponding author: Wei Lin,** Laboratory of Reservoir Microstructure Evolution and Digital Characterization, School of Geosciences, Yangtze University, Wuhan, 430100, China; Institute of Digital Geology and Energy, Linyi University, Linyi, 276000, China; School of Resources and Environment (College of Carbon Neutrality), Linyi University, Linyi, 276000, China, e-mail: ucaslinwei@126.com
Benqiang Wang: Shale Gas Exploration and Development Project Management Department, CNPC Chuanqing Drilling Engineering Company Limited, Chengdu, 610056, China
Denglin Han, Xin Nie, Chenchen Wang, Jizhen Zhang: Laboratory of Reservoir Microstructure Evolution and Digital Characterization, School of Geosciences, Yangtze University, Wuhan, 430100, China

impact on the flow of shale gas, thereby affecting shale gas production [7–9]. Therefore, it is crucial to conduct research on the two-phase gas–water seepage behavior in shale reservoirs.

Shale typically contains organic pores, inorganic pores, and microfractures, which collectively constitute the spatial characteristics of shale gas occurrence and migration. Previous studies have conducted laboratory experiments and simulation research on the seepage behavior of shale gas in different reservoir spaces [10–15]. Deng *et al.* [12] established a quasi-static dual-porosity dual-permeability network model suitable for simulating flow in tight rock and soil media. They analyzed the slippage effect and conducted simulations on the permeability and production characteristics of shale gas. Liu *et al.* [13], based on the dual-medium theory, introduced the anisotropy of fracture normal elastic modulus and permeability. They derived expressions for porosity and permeability of the matrix and fractures, and developed numerical simulations for shale gas reservoirs considering the coupled flow and solid exchange equations for desorption and adsorption. Jun *et al.* [14] employed the lattice Boltzmann method for non-ideal gas, considering the Knudsen layer effect and microscale effects. They used a two-dimensional plate model with slip boundary conditions combining specular reflection and bounce-back formats. The study investigated the influence of factors such as pore size, pressure, and temperature on the micro-scale seepage of shale gas and analyzed the underlying mechanisms. Gao [15] developed a simplified flow rate model for shale gas seepage based on the dust gas model. The model considered the complex pore structure of shale, the slippage effect on the nanoscale pore surface, and diffusion in the matrix system.

In addition to the impact of pore structure on the two-phase flow in shale, reservoir wettability also plays a crucial role in shale two-phase flow. Zheng *et al.* [16] studied the wettability characteristics of the Wind City Formation shale in the Mahu Depression of the Junggar Basin. They comprehensively investigated the wettability features of the shale reservoir and its controlling factors using various experimental techniques such as contact angle measurements, spontaneous imbibition, and micro-CT analysis. Li [17] focused on the coal-permian Shanxi-Taiyuan Formation transitional shale in the southern North China Basin. Through experimental analysis based on shale pore structure tests, wettability tests, and high-pressure methane adsorption, the study extensively explored the wettability characteristics, controlling factors, the impact of wettability on water content and pore parameters, and the controlling mechanisms of wettability on methane adsorption, which are crucial factors affecting shale gas occurrence and production. Ye *et al.* [18] conducted spontaneous imbibition experiments using shale powder devices in both shale oil and gas systems and gas–water systems, further analyzing the imbibition characteristics of shale reservoirs. Liu *et al.* [19] performed a series of wettability experiments on outcrops and core samples of the Longmaxi Formation shale in the Sichuan Basin. The results indicated that the Longmaxi Formation shale surface exhibited both oil-wet and water-wet characteristics, with a preference for oil-wetness. The shale pore surface showed non-uniform wettability. The water-wet surface of shale could lead to water blockages, while the oil-wet surface could alleviate water blockage damage and exhibit strong adsorption capacity for gaseous hydrocarbons.

In summary, previous studies have conducted extensive laboratory experiments and numerical simulations on single-phase flow and two-phase flow of shale gas. However, the micro-scale seepage behavior of gas and water in organic pores, inorganic pores, and microfractures of shale under different wettability conditions has not been fully revealed.

2 Methods

2.1 Digital rock technology

With the continuous development of computer technology and image analysis techniques, digital rock technology has been widely applied in the analysis of porous media, including pore structure, distribution, and micro-scale seepage.

The construction methods of digital rock mainly include two categories: physical experimental methods and numerical reconstruction methods. Numerical reconstruction methods, such as the four-parameter random growth method [20], sequential indicator simulation method [21], simulated annealing method [22], multipoint statistics method [23], and Markov chain-Monte Carlo method [24], although cost-effective, have limitations in terms of accuracy and simulation fidelity due to their reliance on numerical calculations for simulating rock structures [25,26].

Among the various physical experimental methods for digital rock reconstruction, direct construction based on core scanning images is considered to be the closest to real cores. The direct construction method based on scanning images primarily utilizes techniques such as micro-CT scanning [27] and focused ion beam-scanning electron microscopy (FIB-SEM) scanning [28]. It processes the two-dimensional slices obtained from the scanned samples and directly constructs the three-dimensional pore structure of the digital rock, enabling research related to pore permeability. This method can capture the real pore structure of the sample, but it requires a large number of scanning images, is time-consuming, costly, and places high demands on computer image processing capabilities.

In this study, a high-resolution FIB-SEM was employed to obtain the actual micro-scale pore-fracture structure of shale; the three-dimensional digital rock models of shale inorganic pores, organic pores, and microfractures were established; and gas-driven water seepage simulation in shale microscopic pore-fracture structure under different wetting conditions was carried out based on the volume fluent model (VOF) method.

2.2 Volume fluent model

Currently, the simulation of two-phase flow at the microscale can be classified into three main categories: pore network modeling [29], lattice Boltzmann method (LBM) [30,31], and flow simulation based on the Navier–Stokes equations [32]. Among the flow simulation methods based on the Navier–Stokes equations, the VOF method is widely used and has matured in describing multiphase flow. The VOF method is not limited by the properties of the multiphase fluids (such as density ratio) and is more suitable for simulating the flow of gas and water. The VOF method, proposed by Hirt *et al.* [32], is a finite element numerical simulation method that adopts the concepts of Donor–Acceptor, upwind characteristics, and the compensation effect for fluid interface reconstruction. The VOF method has been extensively applied in various fluid simulations both domestically and internationally [33–39].

The basic principle of the VOF method is to divide the fluid within each grid cell and solve the volume fraction function F to track the fluid changes. The free surface is constructed and tracked based on the volume fraction function F. This characteristic reduces the computational resource requirements and memory consumption of the VOF method. For the volume fraction function F, if $F = 1$, the grid cell is entirely occupied by the designated fluid phase (gas or water); if $F = 0$, the grid cell is completely devoid of any designated fluid phase. When $0 < F < 1$, the cell is considered as an interface cell. Assuming an arbitrary point (x, y) in the flow field, the function $f(x, y, t)$ is defined as follows [39]:

$$f(x,y,t) = \begin{cases} 1 \text{ At point}(x,y)\text{,there is a fluid particle of} \\ \quad \text{this phase} \\ 0 \text{ At point}(x,y)\text{,there is a fluid particle of} \\ \quad \text{this phase} \end{cases}. \tag{1}$$

The conservation form of the transfer equation is as follows:

$$\frac{\partial f}{\partial t} + \frac{\partial uf}{\partial x} + \frac{\partial vf}{\partial y} = 0. \tag{2}$$

The time adopts a first-order difference format, and Eq. (2) has the difference form as follows:

$$\frac{F_{i,j}{}^{n+1} - F_{i,j}{}^{n}}{\Delta t} + \frac{\delta F_{i+\frac{1}{2},j} - \delta F_{i-\frac{1}{2},j}}{\Delta x_i} + \frac{\delta F_{i,j+\frac{1}{2}} - \delta F_{i,j-\frac{1}{2}}}{\Delta y_j} = 0. \tag{3}$$

Among them, $\delta F_{i\pm\frac{1}{2},j}$ and $\delta F_{i,j\pm\frac{1}{2}}$ are the flow rates passing through the boundary of the grid element, and its integral form is as follows:

$$\begin{cases} \delta F_{i\pm\frac{1}{2},j} = \dfrac{1}{\Delta t \Delta y_j} \int \mathrm{d}t \int \Delta_{\Delta y_j} (uf)_{i\pm\frac{1}{2},j} \mathrm{d}y \\ \delta F_{i,j\pm\frac{1}{2}} = \dfrac{1}{\Delta t \Delta x_i} \int \mathrm{d}t \int \Delta x_i (uf)_{i,j\pm\frac{1}{2}} \mathrm{d}x \end{cases}. \tag{4}$$

This study uses the VOF method to simulate the gas–water two-phase flow in porous rock media, satisfying the continuity equation and N–S equation. However, the differences from the conventional continuity equation are as follows:

$$\frac{\delta p}{\delta t} + \operatorname{div}(pu) = 0, \tag{5}$$

$$\frac{\mathrm{d}u}{\mathrm{d}t} = f - \frac{1}{\rho} \mathrm{grand} p + v^2 u + S, \tag{6}$$

where u is the dynamic viscosity coefficient (m^2/s); V is the average velocity (m/s); T is the time (s); P is the pressure on the fluid unit (Pa); and S is the source term of seepage resistance, consisting of viscous resistance term and inertial resistance term.

$$S = -\left(\sum_{j=1}^{3} C_{ij} \frac{1}{2} \rho |V| V_j + \sum_{j=1}^{3} D_{ij} u v_j \right). \tag{7}$$

where $\sum_{j=1}^{3} C_{ij} \frac{1}{2} \rho / V / V_j$ is the inertial resistance term; $\sum_{j=1}^{3} D_{ij} u v_j$ is the viscous resistance term; ρ is the density of the fluid (kg/m^3); and C and D are the matrices.

The calculation formula for the viscous resistance coefficient is as follows:

$$\frac{1}{a} = \frac{g}{ku}, \tag{8}$$

where k is the set permeability coefficient; $1/a$ is determined by weighting the volume fraction of the constituent fluid.

The surface tension formula is as follows:

$$F_\sigma = \sigma \kappa \frac{\rho \nabla C}{0.5(\rho_w + \rho_o)}, \tag{9}$$

where σ is the surface tension coefficient and κ is the curvature of the interface.

3 Data setting

3.1 Data source

In this study, FIB-SEM scanning was carried out on the shale samples from the first sub-member of the first member of Silurian Longmaxi Formation in the Weiyuan area. The scanning resolution was set at 5 nm/pixel. Figure 1 shows the original grayscale image obtained from the scanning, which contains the micro-scale pore-fracture structure of the shale. For more detailed information, please refer to Table 1.

Image data information for shale micro-scale structures are shown in Table 1.

The watershed algorithm [40] was employed to segment and binarize the two-dimensional sliced images containing shale organic pores, inorganic pores, and microfractures. The segmented images were then overlaid to generate a three-dimensional digital rock model consisting of only rock pores and the skeleton, as depicted in Figure 2. The connectivity analysis of the digital rock model was conducted using the region filling algorithm [41], and the results are presented in Table 2.

3.2 Model setting

Throughout the simulation process, two-phase flow of gas and water was achieved by relying on capillary forces and a fixed flow rate at the inlet, with the gas phase only infiltrating from one end of the digital rock model. As a result, each cross-section of the different digital rock models only had two opposing permeable boundaries: the interface at the inlet and the interface at the outlet in the initial state. The remaining cross-sections were considered as periodic boundaries to maintain the overall fluid mass balance of the model. The boundary settings for the two-phase flow simulation are illustrated in Figure 3, where the gray area

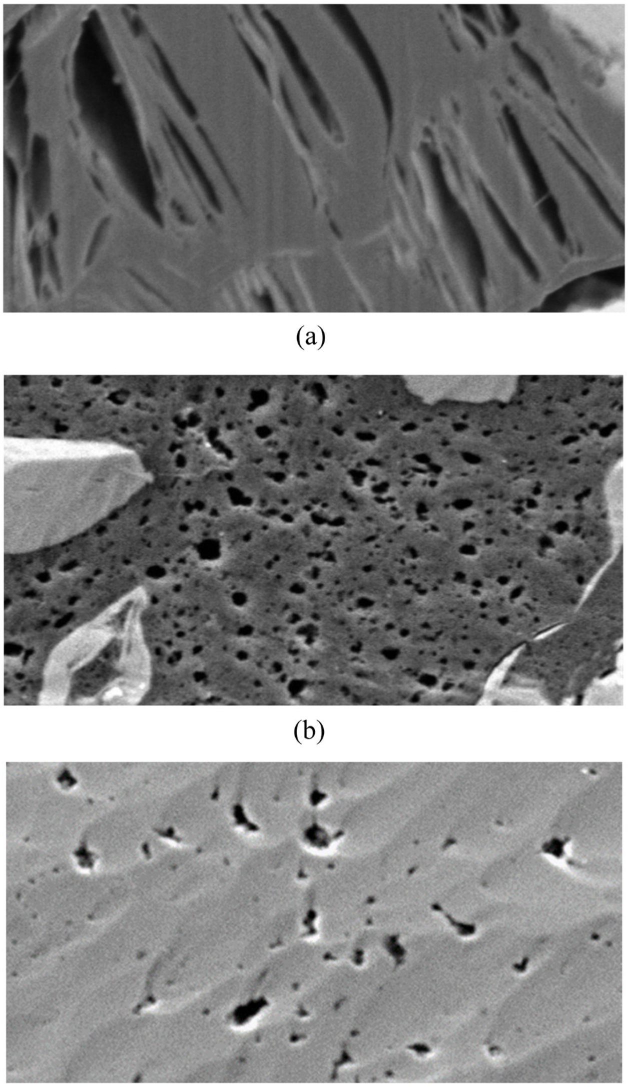
(a)

(b)

(c)

Figure 1: 2D slice image of shale microscopic pores and slits: (a) shale microfracture structure, (b) shale organic pore structure, and (c) shale inorganic pore structure.

Table 1: Image data information

Shale microstructure	Image size (in pixels)	Image resolution (nm/pixel)
Organic pores	1,000 × 500 × 500	5
Inorganic pores	1,000 × 500 × 500	5
Microfractures	1,000 × 500 × 500	5

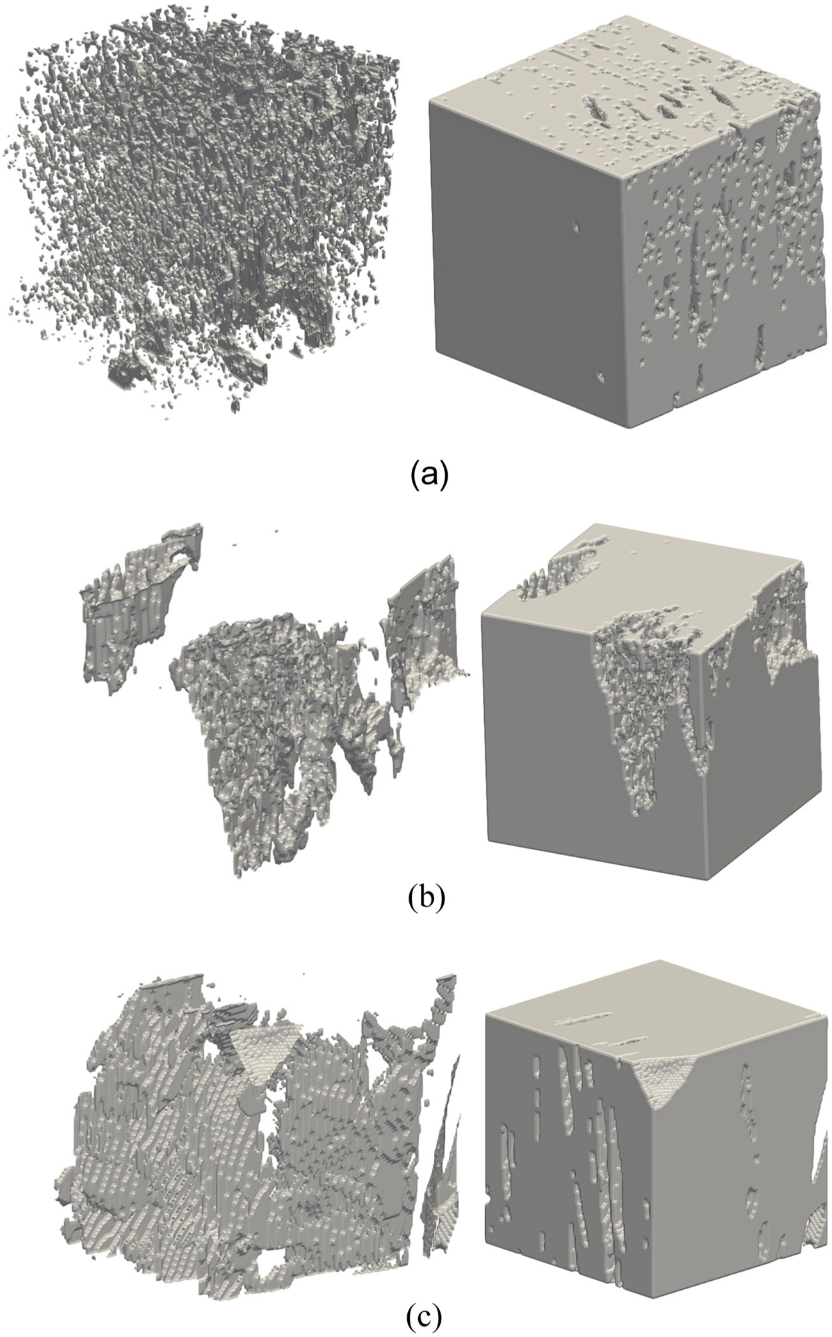

Figure 2: 3D rendering of pore space (left) and rock skeleton (right): (a) three-dimensional digital rock model of inorganic pores, (b) three-dimensional digital rock model of organic pores, and (c) three-dimensional digital rock model of microfractures.

Table 2: Connectivity analysis

Shale microstructure	Porosity (%)	Connected porosity (%)	Isolated porosity (%)
Organic pores digital rock	6.86	4.24	2.62
Inorganic pores digital rock	6.38	5.12	1.26
Microfractures digital rock	6.75	5.55	1.20

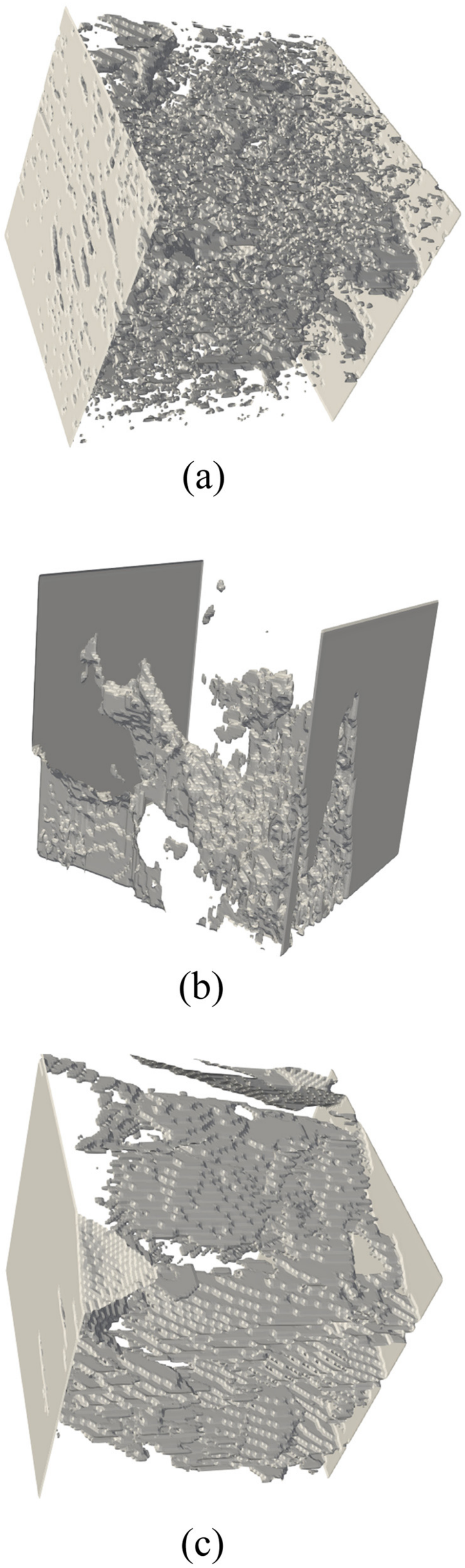

Figure 3: Two-phase seepage simulation boundary: (a) organic pores digital rock, (b) inorganic pores digital rock, and (c) microfractures digital rock.

represents the pore space, the two side plates represent the boundaries, and the rest are non-flowable voxels.

A two-phase gas–water flow simulation was conducted using the VOF method for different pore-fracture structure models under various wettability conditions. The relevant parameter settings are presented in Table 3. The parameter settings were primarily determined based on references from previous studies [36–39]. In the simulation, the gas phase was initially located at the inlet, while the water phase completely saturated the digital rock model. The stopping criterion for the algorithm iteration was set as a water saturation change rate below 0.001 within 20,000 computational time steps, indicating equilibrium in the displacement simulation.

Refine level: the number of refinement levels for the mesh around the interface. cPc: the coefficient for the pressure correction term in the momentum equation. cAlpha: the coefficient for the artificial compression term in the volume fraction equation. Smoothing Kernel: the type of smoothing kernel used to calculate the interface curvature from the volume fraction field. Ufilter1: a parameter that indicates to apply a filtering operation to the velocity field after each time step. Max DeltaT: the maximum allowable time step size for the simulation.

4 Result and discussion

This study simulated the gas–water flow in organic pores, inorganic pores, and microfractures under four different wetting conditions: 15°, 30°, 45°, and 60° contact angles.

Table 3: Parameter settings

Properties	**Water phase**	**Gas phase**
Density	1,000 kg/m^3	1.0 kg/m^3
Viscosity	2.98 mPa s	0.011607 mPa s
Interfacial tension interfacial tension	0.04 N/m	
UD1s	1,000 (μm/s)	
UD0s	1,000 (μm/s)	
Refine level	2.4	
cPc	0.2	
cAlpha	1	
cPc correction	1	
Smoothing kernel	12	
Wall smoothing kernel	0	
Ufilter1	0.015	
max DeltaT	1×10^{-5}	

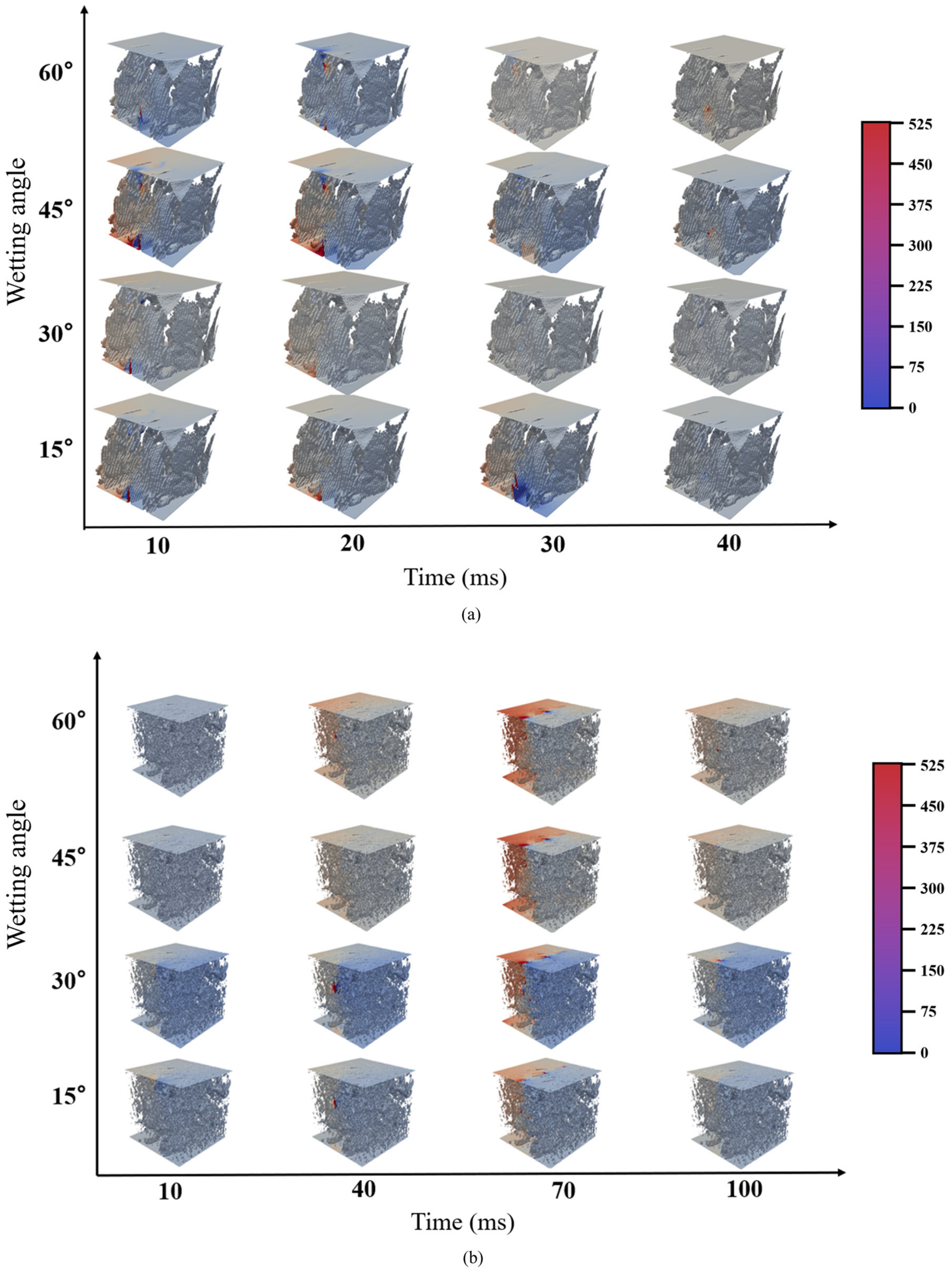

Figure 4: Two-phase seepage process of gas-driven water: (a) microfracture structure, (b) inorganic pore structure, (c) organic pore structure (with a contact angle less than 90°), and (d) organic pore structure (with a contact angle more than 90°).

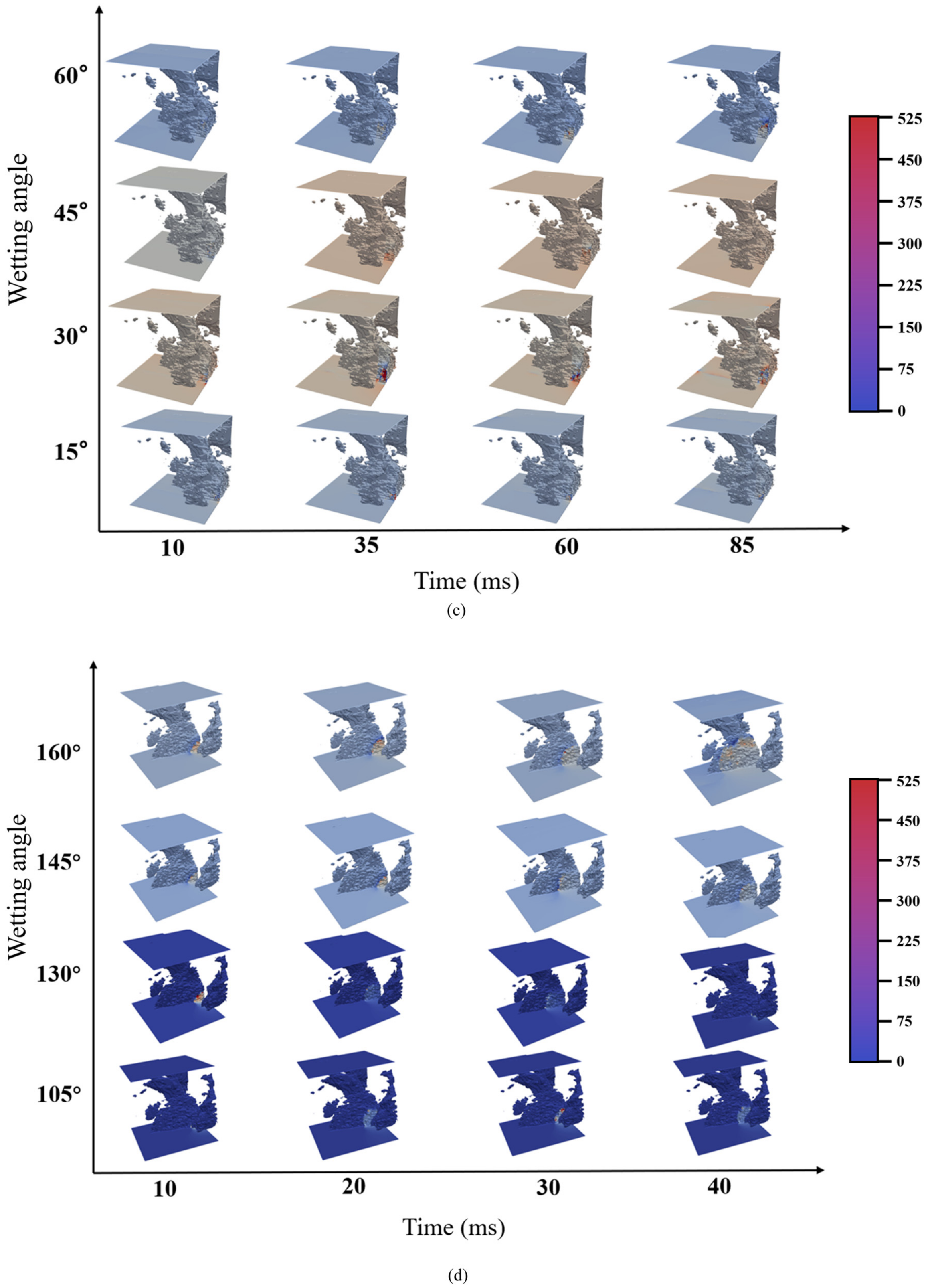

Figure 4: (*Continued*)

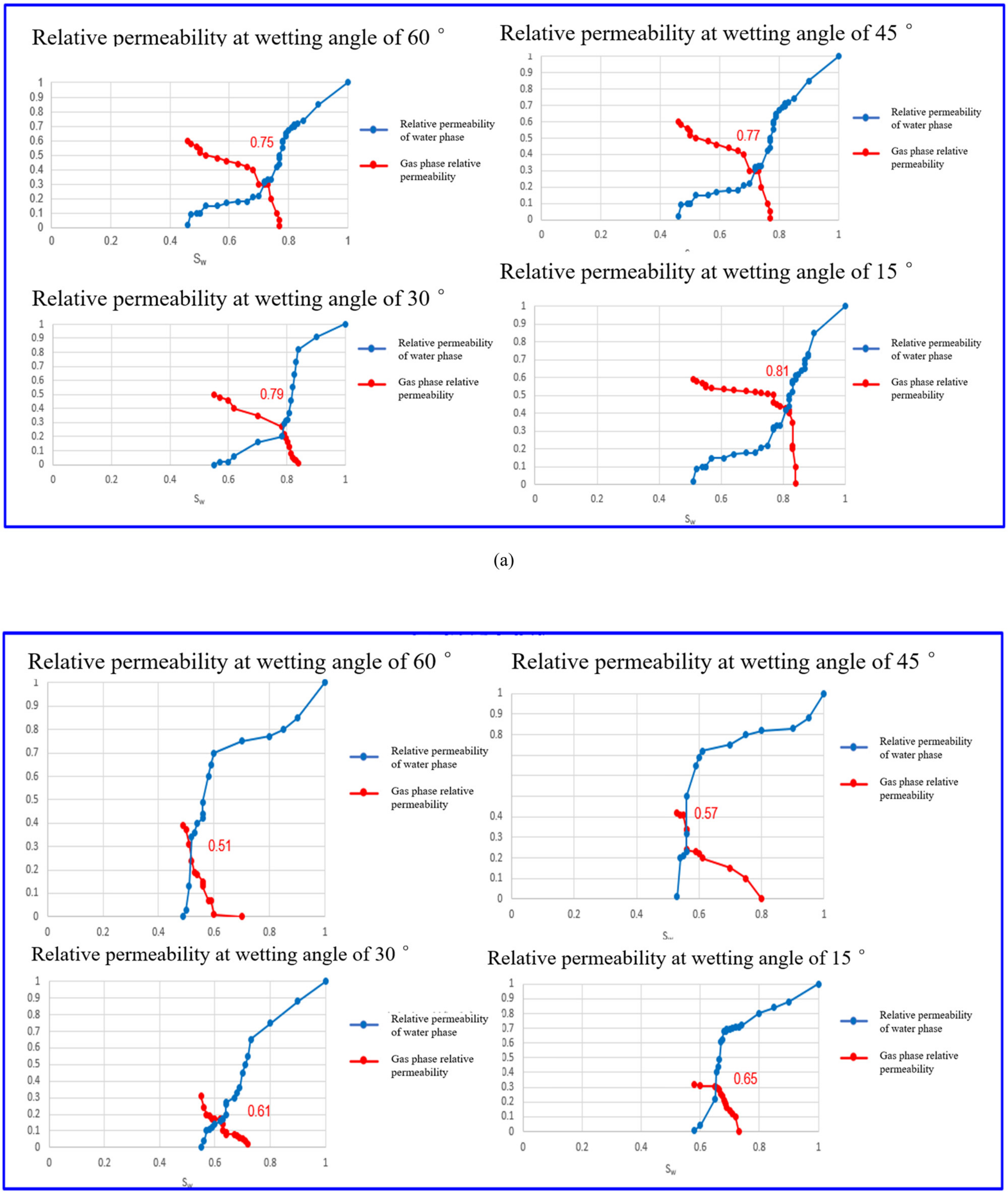

(a)

(b)

Figure 5: Relative permeability curve of gas-driven water: (a) microfracture structure, (b) organic pores digital rock, (c) organic pore structure (with a contact angle less than 90°), and (d) organic pore structure (with a contact angle more than 90°).

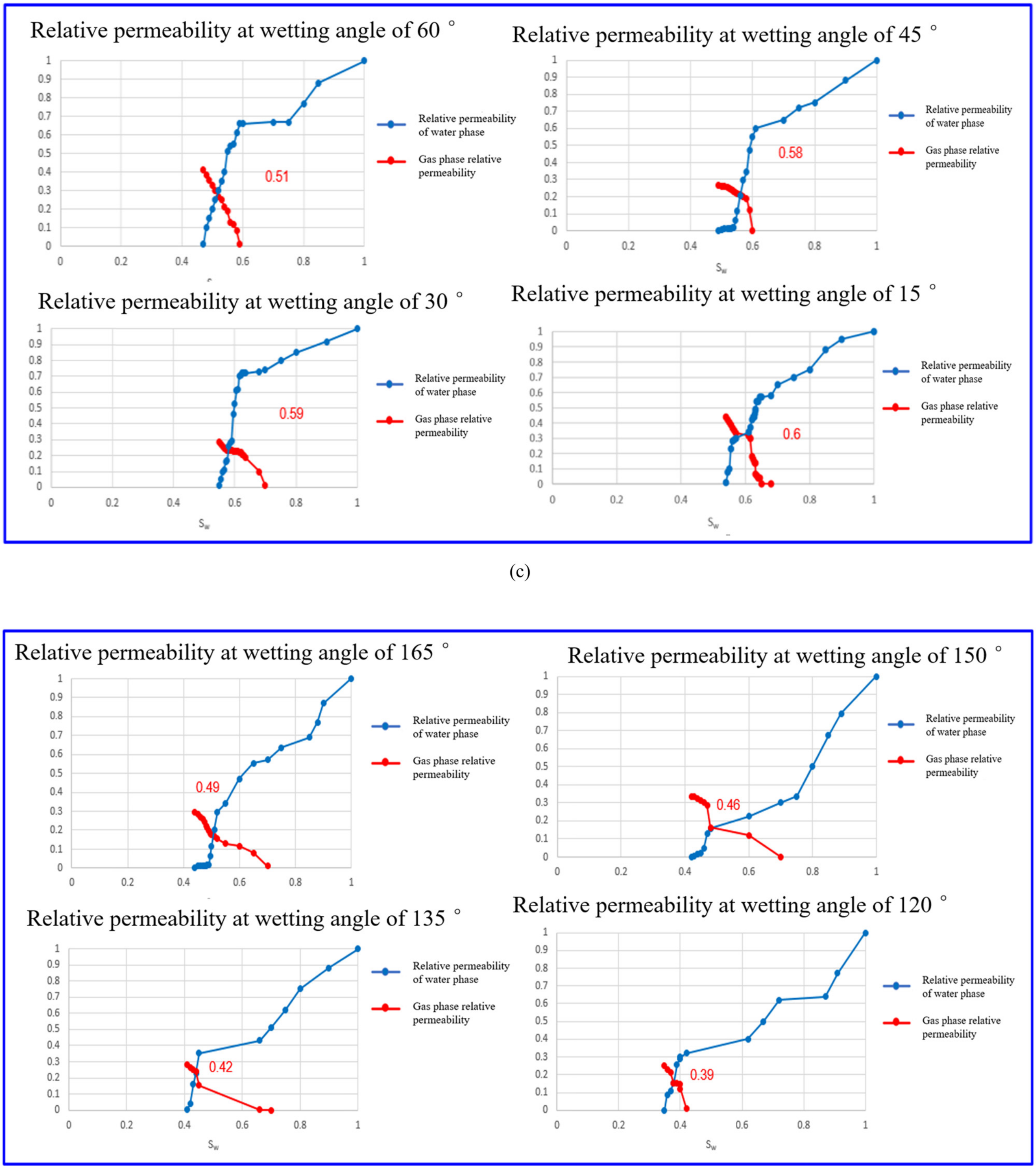

(c)

(d)

Figure 5: (*Continued*)

Additionally, considering the gas-wetting characteristics of organic pores, the gas–water flow in organic pores was separately simulated under four different gas-wetting conditions: 120°, 135°, 150°, and 165° contact angles. Figure 4 illustrates the gas–water flow process in the pore-fracture structure models under different wetting conditions at different time intervals, with each interval representing one-fourth of the total simulation time. The color temperature represents the magnitude of flow velocity, with red indicating areas of high flow velocity and blue indicating areas of low flow velocity.

From Figure 4, it can be observed that the velocity of two-phase flow is highest in water-wet fractures, followed by water-wet inorganic pores and water-wet organic pores, while the velocity is lowest in gas-wet organic pores. Under water-wetting conditions, the variation in the velocity of two-phase flow is most significant in fractures when the contact angle is 45°. When the contact angle is 30°, the variation in the velocity of two-phase flow is most significant in organic pores and inorganic pores. Under gas-wetting conditions, the variation in the velocity of two-phase flow is most significant in organic pores when the contact angle is 165°. The changes in contact angle result in velocity fluctuations primarily at the inlet and outlet of the model and in narrow pore spaces.

From Figure 5, it can be observed that under water-wetting conditions, the relative permeability curves of the fracture structure exhibit an upward concave shape. With an increase in water saturation, the relative permeability of the gas phase initially decreases sharply, followed by a slower decline until reaching the saturation point, after which it decreases sharply again. The range of the saturation point for the fracture structure is between 0.76 and 0.81, with a small variation. As the wetting increases, the saturation point shifts to the right. The two-phase flow region of the fracture structure is larger than that of the organic/inorganic pore structure, and the critical gas saturation is approximately 13%. Under water-wetting conditions, the relative permeability curves of the inorganic pore structure exhibit an upward convex shape, with the gas phase relative permeability gradually decreasing as the water saturation increases. The range of the saturation point for the inorganic pore structure is between 0.51 and 0.65, shifting to the right with enhanced wetting. The critical gas saturation for the inorganic pore structure is approximately 31.5%. Under water-wetting conditions, the relative permeability curves of the organic pore structure also exhibit an upward convex shape, with the gas phase relative permeability decreasing as the water saturation increases. The range of the saturation point for the organic pore structure is between 0.51 and 0.6, shifting to the right with enhanced wetting. The critical gas saturation for the organic pore structure is approximately 34%. Under gas-wetting conditions, the range of the saturation point for the organic pore structure is between 0.39 and 0.49, shifting to the left with enhanced wetting. The critical gas saturation for the organic pore structure is approximately 52.5%.

5 Conclusion

With variations in wettability, the range of saturation point changes was the largest for the inorganic pore structure, followed by the organic pore structure, with the smallest range observed for the fractures. This indicates that the fracture structure is less sensitive to changes in wettability compared to the pore structures. Compared to pore structures, fractures exhibit a larger two-phase flow region, higher saturation point, and lower critical gas saturation. This may be attributed to the larger flow channels and better connectivity provided by fractures, which facilitate the formation of continuous gas–water phases within the fractures, while pore structures are more prone to trapping and Jamin effects. Among the three structures – fractures, organic pores, and inorganic pores – the critical gas saturation for two-phase flow is smallest in water-wet fractures (approximately 13%) and largest in gas-wet organic pores (approximately 52.5%). The critical gas saturation for water-wet organic pores is approximately 34%, which is comparable to that of water-wet inorganic pores (approximately 31.5%). This indicates that by altering the wettability of organic pores in shale, the flow capacity and recovery efficiency of shale gas can be improved.

Funding information: This work is funded by the CNPC Innovation Found (2022DQ02-0102).

Author contributions: All authors have accepted responsibility for the entire content of this manuscript and approved its submission.

Conflict of interest: The authors state no conflict of interest.

Data availability statement: The data used to support the findings of this study are available from the corresponding author upon request.

References

[1] Xinhua MA, Xizhe LI, Liang F, Yujin WAN, Qiang S, Yunghui WANG, et al. Dominating factors on well productivity and development strategies optimization in Weiyuan shale gas play, Sichuan Basin, SW China. Pet Explor Dev. 2020;47(3):555–63.

[2] Tang X, Jiang Z, Li Z, Gao Z, Bai Y, Zhao S, Feng J. The effect of the variation in material composition on the heterogeneous pore structure of high-maturity shale of the Silurian Longmaxi formation in the southeastern Sichuan Basin, China. J Nat Gas Sci Eng. 2015;23:464–73.

[3] Jia YQ, Liu ZP, Ren XH, Zhou YB, Zheng AL, Zhang J, et al. Organic matter type differentiation process and main control mechanism: Case study of the Silurian Longmaxi formation shale reservoir in Weiyuan area. Acta Sedimentol Sin. 2021;39(2):341–52.

[4] Yanchao L, Zhang Q, Jianguo S. Volumetric stimulation technology of long-section multi-cluster temporary plugging in shale gas reservoirs. Nat Gas Ind. 2022;42(2):143–50.

[5] Zhiliang H, Haikuan N, Dongfeng H, Tingxue J, Ruyue W, Yuying Z, et al. Geological problems in the effective development of deep shale gas: a case study of Upper Ordovician Wufeng-Lower Silurian Longmaxi formations in Sichuan Basin and its periphery. Acta Pet Sin. 2020;41(4):379–91.

[6] Wan Y, Li Z, Lu B. The development of Fayetteville shale play and its implications. Nat Gas Geosci. 2019;30(11):1655–66.

[7] Liu N, Liu M, Zhang S. Flowback patterns of fractured shale gas wells. Nat Gas Ind. 2015;35(3):50–4.

[8] Gang L. Research on accurate metering of flowback fluid after shale gas fracturing in Changning-Weiyuan block. Drilling Prod Technol. 2019;42(3):57–60.

[9] Lu Y, Wang H, Guan B, Liu P, Guo L, Wu J, et al. Reasons for the low flowback rates of fracturing fluids in marine shale. Nat Gas Ind. 2017;37(7):46–51.

[10] Li Y, Liu X, Hu Z, Gao SS, Duan XG, Chang J. A new method for the transport mechanism coupling of shale gas slippage and diffusion. Acta Phys Sin. 2017;66(11):230–40.

[11] Yang YF, Wang CC, Yao J, Hu RR, Sun H, Zhao JL. A new method for microscopic pore structure analysis in shale matrix. Earth Sci. 2015;36(10):1280–9.

[12] Deng S, Lu L, Liu H. Pore-fractural network model for compacted geomaterials and simulation of shale gas seepage. Chin J Undergr Space Eng. 2015;11(S1):76–9.

[13] Liu WQ, Wang DN, Su Q. Dual media model of shale layer with anisotropy involved and its simulation on gas migration. Nat Gas Geosci. 2016;27(8):1374–9.

[14] Jun Y, Jianlin Z, Min Z, Lei Z, Yongfei Y, Zhixue S, et al. Microscale shale gas flow simulation based on Lattice Boltzmann method. Acta Pet Sin. 2015;36(10):1280–9.

[15] Jun G. Gas flow characteristics of unsaturated shale: a study case in the eastern Qaidam Basin in China. Beijing: China University of Geosciences (Beijing); 2017.

[16] Zheng G, Gao Z, Huang L, Jiang Z, He W, Chang J, et al. Wettability of the Permian Fengcheng Formation shale in the Mahu Sag, Junggar Basin, and its main control factors. Oil Gas Geol. 2022;43(5):1206–20.

[17] Pei L. Wettability of shale and its effect on methane adsorption:a case study of Shanxi and Taiyuan formations in southern north China basin. Beijing: China University of Geosciences (Beijing); 2021.

[18] Ye H, Ning Z, Wang Q, Cheng Z, Huang L, Mu D. Spontaneous imbibition experiment and wettability of shale reservoir. Fault-Block Oil Gas Field. 2019;26(1):84–7.

[19] Liu X, Xiong J, Liang L, Luo C, Zhang A. Analysis of the wettability of Longmaxi formation shale in the south region of Sichuan basin and its influence. Nat Gas Geosci. 2014;25(10):1644–52.

[20] Wang M, Wang J, Pan N, Chen S. Mesoscopic predictions of the effective thermal conductivity for microscale random porous media. Phys Rev E. 2007;75(3):036702–12.

[21] Xuefeng L, Jianmeng S, Haitao W, Huawei YU. The accuracy evaluation on 3D digital cores reconstructed by sequence indicator simulation. Acta Pet Sin. 2009;30(3):391–5.

[22] Wang C, Yao J, Yang Y, Zhang L, Pang P, Yan Y. Percolation properties analysis of carbonate digital core based on lattice Boltzmann method. J China Univ Pet (Sci. Technol. Ed.). 2012;36(6):94–8.

[23] Pang W. Reconstruction of digital shale cores using multi-point geostatistics. Nat Gas Ind. 2017;37(9):71–8.

[24] Wu K, Nunan N, Crawford JW, Young IM, Ritz K. An efficient Markov chain model for the simulation of heterogeneous soil structure. Soil Sci Soc Am J. 2004;68(2):346–51.

[25] Wei L, Xizhe L, Zhengming Y. Digital rock construction and microscopic seepage simulation of tight oil reservoirs. Beijing: Petroleum Industry Press; 2021.

[26] Lin W, Li X, Yang Z, Manga M, Fu X, Xiong S, et al. Multiscale digital porous rock reconstruction using template matching. Water Resour Res. 2019;55(8):6911–22.

[27] Lin W, Wu Z, Li X, Yang Z, Hu M, Han D, et al. Digital characterization and fractal quantification of the pore structures of tight sandstone at multiple scales. J Pet Explor Prod Technol. 2022;(12):2565–75.

[28] Yang Y, Liu F, Yao J, Song H, Wang M. Reconstruction of 3D shale digital rock based on generative adversarial network. J Southwest Pet Univ (Science& Technol Ed). 2021;43(5):73–83.

[29] Blunt M. Flow in porous media– pore-network models and multiphase flow. Curr Opin Colloid Interface Sci. 2001;6(3):197–207.

[30] Xie C, Raeini AQ, Wang Y, Blunt MJ, Wang M. An improved pore-network model including viscous coupling effects using direct simulation by the lattice Boltzmann method. Adv Water Resour. 2017;100:26–34.

[31] Lin W, Xiong S, Liu Y, He Y, Chu S, Liu S. Spontaneous imbibition in tight porous media with different wettability: Pore-scale simulation. Phys Fluids. 2021;33(3):032013.

[32] Hirt CW, Nichols BD. Volume of fluid (VOF) method for the dynamics of free boundaries. J Comput Phys. 1981;39(1):201–25.

[33] Malgarinos I, Nikolopoulos N, Marengo M, Antonini C, Gavaises M. VOF simulations of the contact angle dynamics during the drop spreading: Standard models and a new wetting force model. Adv Colloid Interface Sci. 2014;212:1–20.

[34] Raeini A, Blunt M, Bijeljic B. Modelling two-phase flow in porous media at the pore scale using the volume-of-fluid method. J Comput Phys. 2012;231:5653–68.

[35] Raeini A, Blunt M, Bijeljic B. Direct simulations of two-phase flow on micro-CT images of porous media and upscaling of pore-scale forces. Adv Water Resour. 2014;74:116–26.

[36] Fuster D, Bagué A, Boeck T, Le Moyne L, Leboissetier A, Popinet S, et al. Simulation of primary atomization with an octree adaptive mesh refinement and VOF method. Int J Multiph Flow. 2009;35(6):550–65.

[37] Liu Z, Sunden B, Yuan J. VOF modeling and analysis of filmwise condensation between vertical parallel plates. Heat Transf Res. 2012;43(1):47–68.

[38] Zhang M, Zhong X, Li G. Application of VOF numerical simulation in seepage problem with complex seepage control structure. Shaanxi Water Resour. 2018;(6):254–7.

[39] Zhang J, Fang J, Fan B. Advances in research of VOF method. Adv Sci Technol Water Resour. 2005;(2):67–70.

[40] Xiang W, Suyun LUO. Watershed segmentation based on region separation and aggregation. Computer Digital Eng. 2021;49(1):190–5.

[41] Longyuan M, Zhenglin Y, Zhen W. Regional filling algorithm based on connected region labeling. J Changchun Univ Sci Technol (Nat Sci Ed). 2018;41:114–7.